The WFPC2 and WFC3 PSF Database

F. Dauphin, J. Anderson, V. Bajaj, L. Dressel, K. Sahu, M. Bourque, C. Shanahan

July 30, 2021

Abstract

Accurate and precise measurements of stellar PSFs (Point Spread Functions) have many applications in astronomy. In order to maximize HST's scientific output, we built libraries of observed stellar PSFs from WFPC2, WFC3/UVIS, and WFC3/IR images. We describe the star-image-extraction pipeline, which involves identifying potential stellar sources in calibrated images and measuring against various PSF models. We report that the mean fractional disagreements between model and image pixels were 0.103±0.030, 0.090±0.076, and 0.046±0.024 for WFPC2, WFC3/UVIS, and WFC3/IR, respectively. We summarize the contents of the database by analyzing several distributions and confirming that these distributions are aligned with expectations. All the images of confirmed stellar sources were uploaded to the Mikulski Archive for Space Telescopes (MAST) along with complimentary metadata obtained from engineering and model-PSF fitting. We also discuss how to retrieve appropriate PSFs for specific applications using the archive. Finally, we discuss key astronomical applications of the database, and future work.

1. Introduction

Astronomical point sources (objects whose true spatial extent is much less than a single resolution element) will appear on the detector as a pattern of pixels, known as a point spread function (PSF). One powerful way to measure an object's total flux is by fitting a PSF. This measurement is particularly useful when the field is crowded because the source fluxes will overlap if one uses too large of a circle to estimate the flux without fitting the PSF. To facilitate users in building PSFs appropriate for their observations, we made a full dataset of observed star images from the Wide Field Planetary Camera 2 (WFPC2) and the Wide Field Camera 3 (WFC3). The database contains approximately 30 million star images (aka PSF realizations); it includes all WFPC2 observations taken from 1993 to 2009 and all WFC3 observations taken from 2009 to 2019. We update the database annually and the database lags by a full year. These resulting PSF realizations may help in accurate, high precision photometry/astrometry for our users' own PSF modeling (https://www.stsci.edu/hst/instrumentation/wfc3/data-analysis/psf/psf-search).

Unfortunately, even though accurate PSF models are critical to many astronomical studies, they are difficult to construct. The WFC3/UVIS detectors are mildly under sampled, which means that an accurate PSF can only be constructed from a dithered set of data, and one must take exquisite care to accurately represent the sub-sampled nature of the PSF. Around 17% to 20% of a star's flux will land on the central pixel if the star is centered on that pixel. However, the IR detector is extremely undersampled, and over 40% of a star's flux will land on the central pixel (Dressel 2021). In addition, the PSF changes with position across the field. These changes are due to variations in optical distortion and variations in the thickness of the detector, which is related to charge diffusion (Krist 2003). Furthermore, the PSF also changes over time due to secular and breathing-related changes in instrument focus (https://www.stsci.edu/hst/instrumentation/wfc3/data-analysis/psf).

Although PSFs are difficult to deal with in practice, they are extremely useful and critical for scientific applications. A library with millions of extracted realizations of the PSF opens numerous scientific possibilities. In particular, the PSF library provides PSFs extending over the full range of model focus values from -19 to 14 microns, and the full area of the detector. The library also provides accurate (typically better than 0.1 pixel) x-coordinate and y-coordinate values of all the PSFs. A set of observed PSFs centered on different parts of a pixel can serve analogous to a dithered set. Thus these PSFs provide an excellent opportunity for users to generate well-sampled PSFs that they can use for their own science.

The report is organized as follows. In Section 2, we introduce our instruments, PSFs, and image databases. In Section 3, we explain our PSF fitting algorithm in detail. In Section

4, we review our results and their implications for the database. In Section 5, we explain how to retrieve PSFs through MAST. In Section 6, we discuss potential uses in research and future work. In Section 7, we end with our conclusions.

2. Instruments and Methods

2.1. Brief Overview of WFPC2 and WFC3

The Wide Field Planetary Camera 2 (WFPC2) is the successor of the Wide Field Planetary Camera (WF/PC). It was installed in 1993 and ended its mission in 2009. It was comprised of three Wide Field Cameras (WFCs) and one Planetary Camera (PC), which are utilized together to take a single image. The Wide Field Camera 3 (WFC3) was installed in 2009 as WFPC2's successor and is currently serving as one of the operating instruments on the Hubble Space Telescope (HST). It has two channels, WFC3/UVIS for the ultraviolet/visible wavelengths and WFC3/IR for the near-infrared wavelengths. Table 1 (McMaster et al. 2010) and Table 2 (Dressel 2021) summarize the main characteristics of these two instruments. More details about the instruments can be found in the first two chapters of their respective instrument handbooks (IHB). For the remainder of this report, "WFC3" will refer to both channels and "WFC3/UVIS" and "WFC3/IR" will be referred to as UVIS and IR.

Camera	Pixel and CCD Format	Field-of-View	Pixel Scale	F/ratio
Wide Field	800×800 $\times$ 3 CCDs	$2.5' \times 2.5'$ (L-shaped)	~100 milli-arcseconds	12.9
Planetary	800×800 $\times$ 1 CCD	$35'' \times 35''$	~46 milli-arcseconds	28.3

Table 1: *Summary of the WFPC2 camera format (McMaster et al. 2010).*

Channel	f-ratio	Detector type	Spectral range (nm)	Detector pixel format	Pixel scale (arcsec)	Field of view (arcsec)
UVIS	31	CCD	200-1000	$2 \times 2051 \times 4096$	0.0395×0.0395	162×162
IR	11	HgCdTe	800-1700	1014×1014	0.135×0.121	136×123

Table 2: *Characteristics of the WFC3 channels (Dressel 2021).*

2.2. PSFs and Photometric Details

A point spread function (PSF) is the apparent surface brightness profile of a point source on the detector (McMaster et al. 2010). A point source's brightest pixel will be in the middle and the fainter pixels will surround it, capturing the spatial distribution of flux. The primary characteristic of a PSF is encircled energy, which is the fraction of the total light from a point source that is contained within a circular aperture of a given radius (Dressel 2021). Figures 1 and 2 illustrate how flux varies with respect to radius on WFPC2 and WFC3 (Dressel 2021, McMaster et al. 2010). HST breathing, or the thermal change in focus on an orbital timescale, affects the PSF as well. This effect is estimated by the HST Focus Model, which we discuss in Section 2.3.
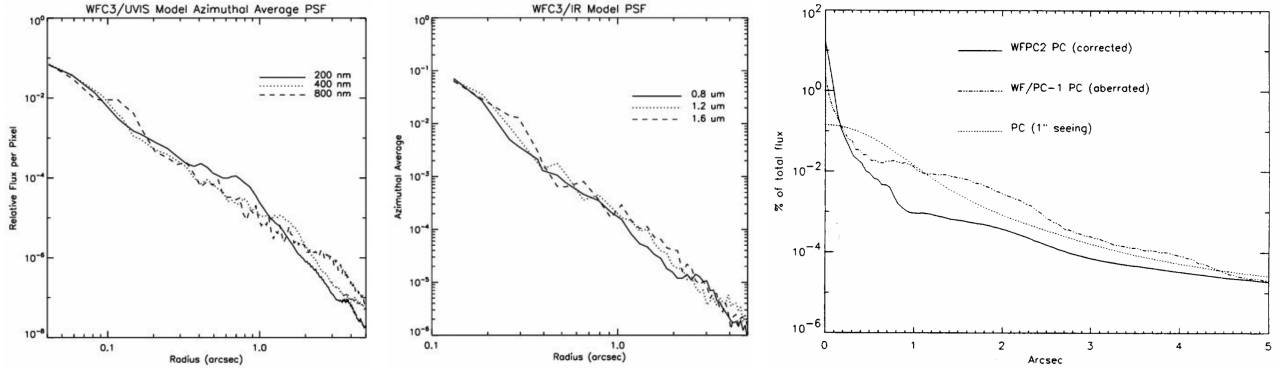

Fig. 1.—*The PSF azimuthal average/surface brightness for WFC3/UVIS, WFC3/IR, and WFPC2 (left to right). WFC3/UVIS displays profiles for 200, 400, and 800 nm. WFC3/IR displays profiles for 800, 1200, and 1600 nm. WFPC2 displays the 400 nm profile (Dressel 2021, McMaster et al. 2010).*
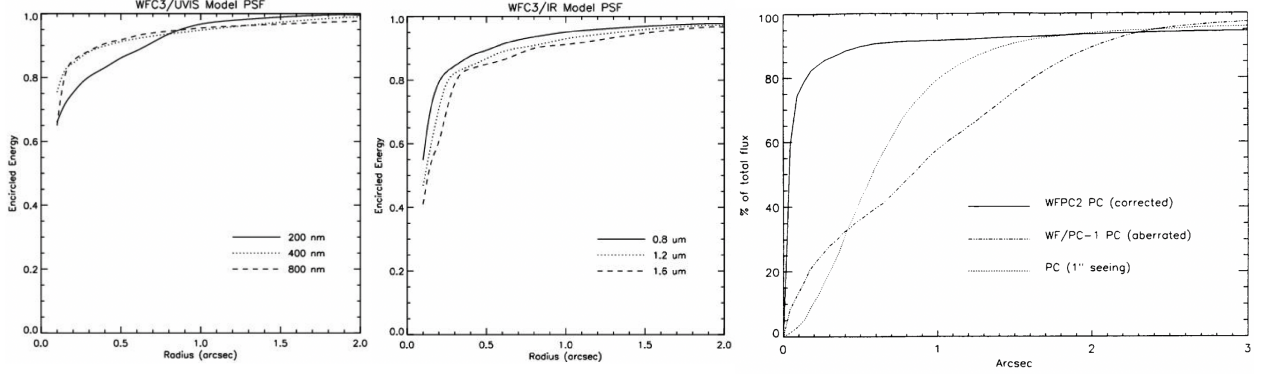
Fig. 2.—*The PSF encircled energy for WFC3/UVIS, WFC3/IR, and WFPC2 (left to right).
Each figure displays profiles for the same respective wavelengths as in the previous figure
(Dressel 2021, McMaster et al. 2010).*

The WFC3 PSF *models* were empirically constructed from well dithered datasets taken
from star cluster Omega Centauri (omega Cen) early in the lifetime of WFC3 (Anderson
2016 & 2018). They were constructed according to the algorithm described in Anderson and
King (2000). The basic PSF model is a 101x101 array that is supersampled by a factor of
four such that it goes to a radius of 12.5 pixels. Bi-cubic interpolation is used to evaluate
the PSF at locations in-between the array points. The WFC3/UVIS detector is modeled
with a 7x8 array of fiducial PSFs across the detector. The WFC3/IR PSF has a 3x3 array
of fiducial PSFs. The WFPC2 PSF models are a 3x3 array of PSFs for each of the four
chips. Figures 3, 4, and 5 display some examples of PSFs for each instrument. The models
are publicly available at https://www.stsci.edu/~jayander/STDPSFs/WFPC2/ and https:
//www.stsci.edu/hst/instrumentation/wfc3/data-analysis/psf under "WFC3/UVIS
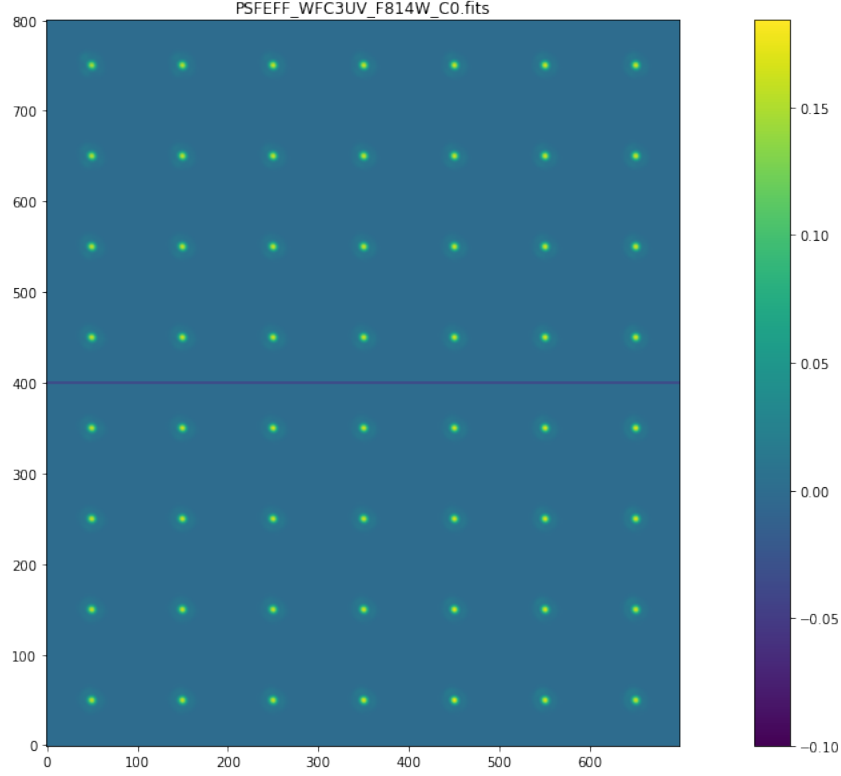PSF Downloads" and "WFC3/IR PSF Downloads".

Fig. 3.—*WFC3/UVIS F814W PSFs. The WFC3/UVIS PSFs are evenly distributed in a 7x4 array for each chip (7x8 overall), which sufficiently represents the spatial variation of the PSF across the detector. The pixel values are the fraction of light that lands in the pixel with respect to where the star lands on the central pixel. They are provided in two formats: a single 2-d image that shows the array of PSFs and the residuals relative to the mean PSF, which is not illustrated (Anderson 2018).*
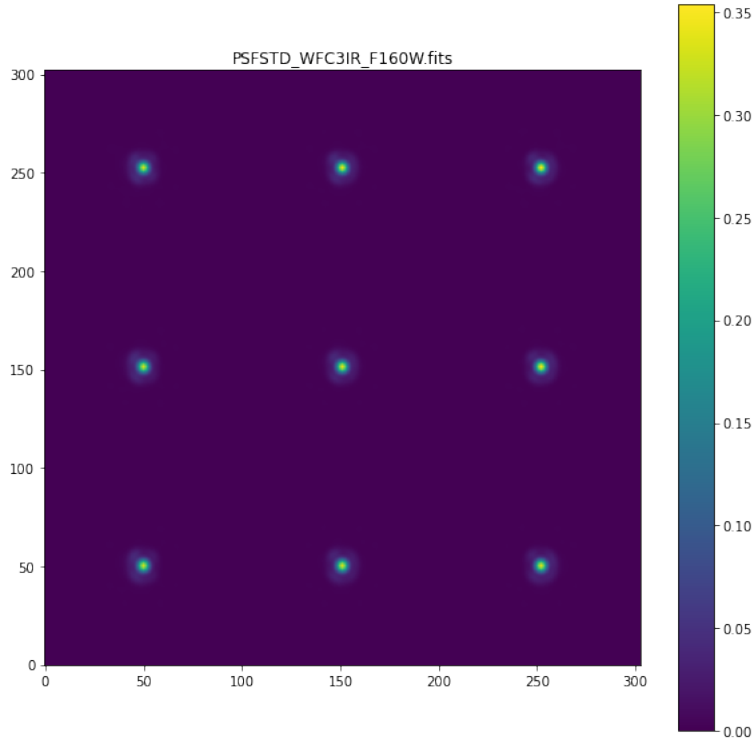
Fig. 4.—*WFC3 IR F160W PSFs. The shape of WFC3/IR PSF* `.fits` *files are (9, 101, 101). The pixel values have the same units as in Figure 3. This figure is displaying each PSF in a 3x3 grid on a 303x303 image. Since the WFC3/IR PSF does not vary with position as much as WFC3/UVIS, we can model its PSF efficiently using 9 rather than 56.*
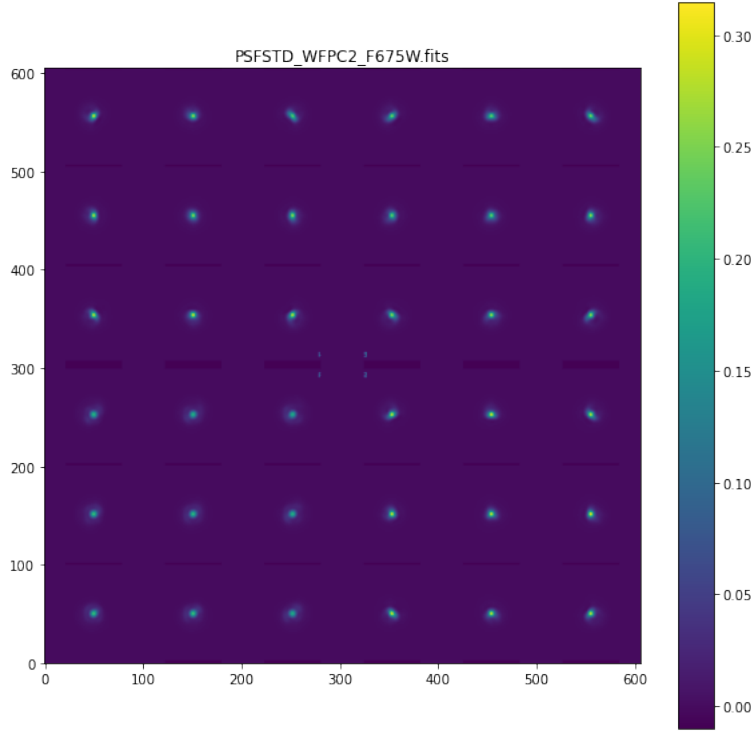
Fig. 5.—*WFPC2 F675W PSFs. The shape of WFPC2 PSF `.fits` files are (36, 101, 101). The pixel values have the same units as in Figure 3. Each 3x3 box (four in total) corresponds to a different camera. This figure is displaying each PSF in a 6x6 grid on a 606x606 image.*

In WFPC2, the cameras bleed almost exclusively along the columns, which results from excessive saturation. If bleeding is expected, it was advised to run serial transfer registers of the CCDs during an exposure so the bleed off charge did not corrupt other parts of the image (McMaster et al. 2010). In addition, diffraction effects from the edges of the shutter blades affected PSFs for very short exposures in WFPC2 (McMaster et al. 2010).

WFC3/UVIS also bleeds along the column when saturated, but WFC3/IR is immune to bleeding because there are no potential barriers between pixels. However, saturation is still a concern because pixels subject to the highest signal levels show higher dark-current rates, or image persistence, in subsequent exposures. For HST, a 2.4-m telescope, operating at 600nm, the diffraction limit is $\theta \approx 1.22\frac{\lambda}{D} = 51$ mas (Dressel 2021). Detailed documentation of the PSFs is provided in WFPC2 IHB Chapter 5 and WFC3 IHB Chapter 6.6 for WFC3/UVIS and 7.6 for WFC3/IR.

2.3. Image and Focus Model Data

All WFPC2 images (approximately 180K) were downloaded from the Mikulski Archive for Space Telescopes (MAST). We also queried MAST to retrieve approximately 146K WFC3/UVIS images and 185K WFC3/IR images that were not proprietary, i.e. those observed before 2020-01-01, for PSF fitting. PSF models are most accurate in the individual flat-fielded frames since the pixel values in these images are our only true and direct constraints when observing astronomical objects. Hence, we used calibrated flat-fielded images (_flt.fits) for WFC3 PSF fitting. We also used calibrated images (_c0m.fits) for WFPC2 PSF fitting, analogous to using _flt.fits images for WFC3.

The HST Focus-Model algorithm estimates the focus value for the telescope approximately every five minutes, taking the average temperature sensor values of the telescope into account (Nino et al. 2008). The model focus is defined as the longitudinal motion of the Secondary Mirror in microns. These values are periodically normalized to the actual focus value measured through phase-retrieval techniques (Dressel, 2012; Sabbi and Bellini, 2013). The focus model data estimated from temperature measurements are only available since 2003 in the engineering data. WFPC2's PSF database utilizes focus data from 2003-2009 and WFC3 utilizes focus data from 2009-present day (https://www.stsci.edu/hst/instrumentation/focus-and-pointing/focus/hst-focus-model). Figures 6 and 7 summarize the focus model data.

Fig. 6.—*Focus model data from Jan 2003 to May 2009 (top) and June 2009 to Dec 2019 (bottom). Around late 2005 and mid-late 2006, there are noticeable gaps where there is no focus model data for a few weeks.*
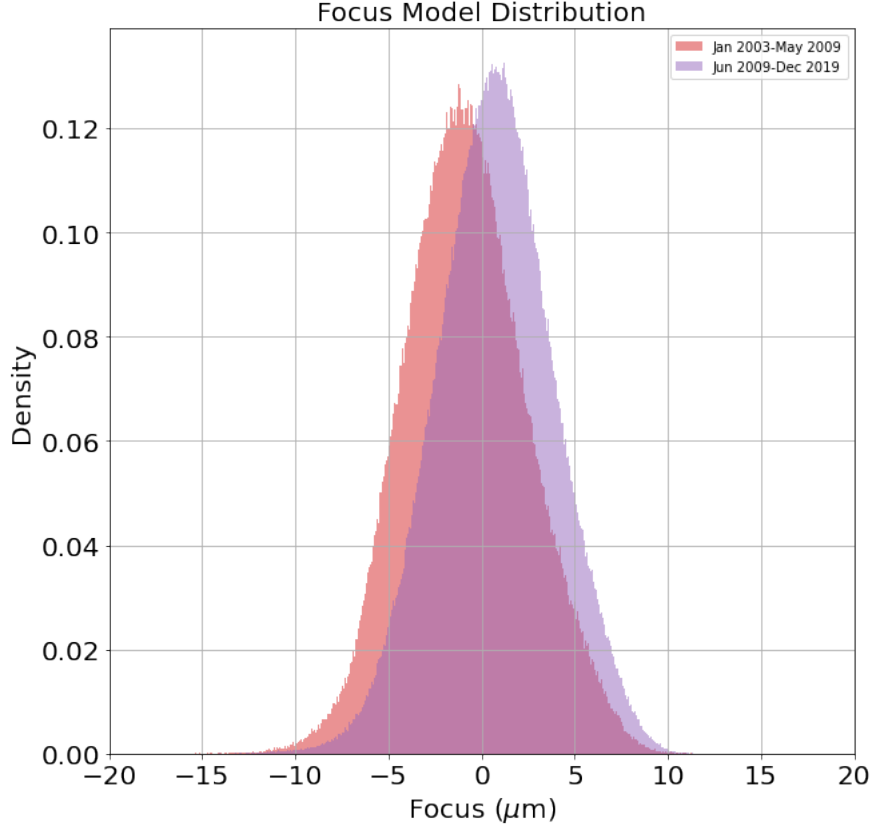
Fig. 7.—*Focus model distributions from Jan 2003 to May 2009 (red) and June 2009 to Dec 2019 (purple). The y-axis is density, which is normalized frequency and makes the integral of each curve equal to one. The focus models are normally distributed, share similar variances, and differ slightly in mean value.*

3. PSF Fitting Algorithm

The `img2xym_wfc3uv` (WFC3/UVIS) and `hst1pass` (WFC3/IR; WFPC2) routines found all the stars in our images that met some simple brightness and isolation criteria (Anderson 2006). It used the library of PSFs provided on the websites in Section 2.2 to measure positions and fluxes for each star. The PSF model used for each image was the model closest in waveband, e.g. IR F164N used model F160W. Note that the routine was designed to measure stars that are relatively isolated. If there are nearby neighbors, e.g. within a few pixels, the finding and measurement of both stars will be compromised. We used an isolation index of 7, which only finds stars in pixels that have no brighter neighbors within 7 pixels. We chose 7 because a significant amount of flux will come from the measured source and

not neighboring stars. The number of stars that fail this requirement are not recorded as metadata. The minimum flux over sky a star must have to be included in the find was 10^4 electrons (e$^-$), which guaranteed the sources had a S/N of ≈ 50 at its center. The maximum flux a single pixel can have to be included was 5.9×10^4 e$^-$, which ensured that there would be no saturated stars in the database. The WFC3/UVIS fits required a mean absolute deviation, or quality of fit, ≤ 0.5 to make it into the final list. WFC3/IR and WFPC2 fits required a quality of fit and similar residual metrics < 0.15 to ensure more confidence in our star selection and restrict our selection to well fit stars. We chose these respective thresholds because they sufficed for capturing all point sources regardless of relative flux.

The final measurable outputs were sky level, x-coordinate & y-coordinate positions, quality of fit ($Qfit$), and flux. The sky level was calculated using a robust sigma clipping average by taking an annulus relative to the star's size as close as possible to the star's central pixel. To find the best position, we used only the inner 5x5 pixels centered on the star's brightest pixel and performed a simple grid search for the position that minimizes the sum of the residuals between the star and the model. We chose a 5x5 box because it contains a majority of the flux and a wide range of pixel-pixel variation. The quality of the PSF fit, $Qfit$, was defined as the sum of the absolute value of the residuals relative to the flux and PSF model within a 5x5 box divided by the total flux over sky within the box. This formulation for fitting error was chosen over a formal chi-squared since such unweighted fractional error tells us more about the PSF-fit independent of the S/N of the stars. We used proper noise-based weighting to measure flux.

For WFC3/UVIS, we removed dark images, guidestar failure images, and certain subarray images, which tended to not have enough stars to be useful. For WFC3/IR, we instead removed certain subarrays, grisms, biases, darks, flats, and guidestar failures from our samples because they were not good for PSF fitting. For WFPC2, we used only external images for PSF fitting since all the other images were internal observations and would not be expected to contain star images.

In addition, we estimated the focus of the images at their MJD using the HST Focus Model. As stated before, the focus model estimates HST's defocus approximately every five minutes. Unfortunately, there are gaps in the focus model data that can be from an hour to a few weeks long (see Figure 6 and Figure 8). If there was no focus data within a 12-minute window of the exposure's MJD, then the image was taken during one of the gaps and returned Null for focus. If there was one focus data value within a 12-minute window of the MJD, then the image was taken at the edge of one of the gaps and the estimated focus was the model measurement. If there were two or more focus data within a 12-minute window of MJD, then the image was not taken near a gap. The estimated focus was the interpolation of the focus values in the window with respect to MJD.
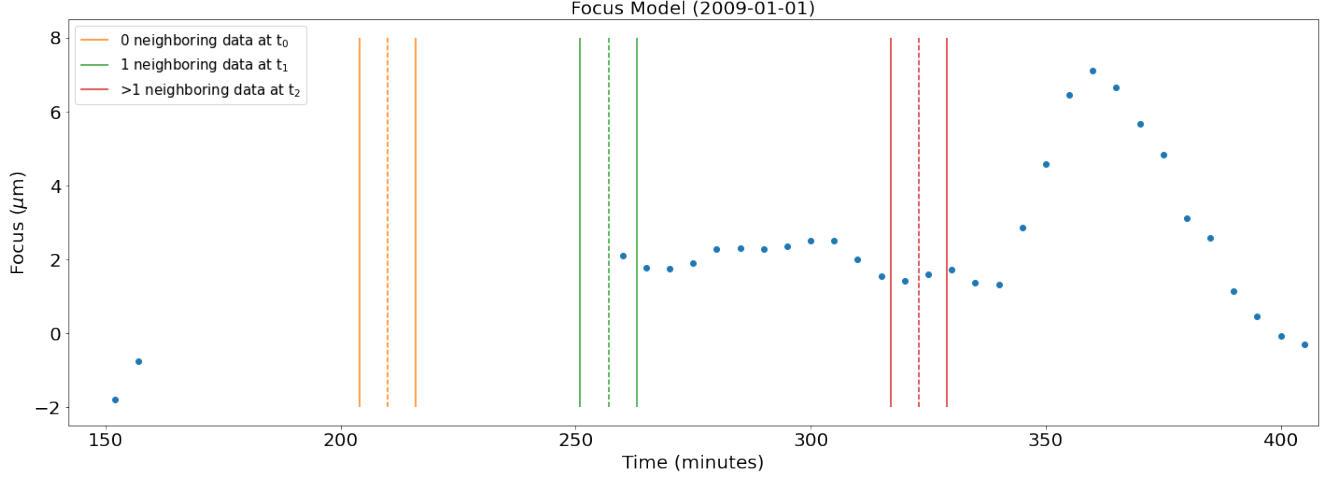
Fig. 8.—*Estimating focus model values. The dashed lines represent observations at t_i and the solid line ranges represent 12 minute windows to search for focus values with respect to t_i. The orange range has no neighboring data so observations at t_0 return a Null focus value. The green range has one neighboring data so observations at t_1 return the single focus value. The red range has multiple neighboring data so observations at t_2 return an estimated focus value from interpolation of the nearby values.*

4. Results

The list below is the following metadata available in the database (https://www.stsci.edu/hst/instrumentation/wfc3/data-analysis/psf/psf-search). Metadata that are seen in all databases are not specified in the list below, e.g. X is used in all databases, but Chip is only used in the WFC3/UVIS database.

- Rootname – Unique image name

- Filter – Filter used (WFC3 used one filter per image, WFPC2 could use two per image)

- Aperture – The active region of the detector to be read out (Dressel 2021)

- X –PSF x center coordinate

- Y –PSF y center coordinate

- Chip – 1 or 2 (WFC3/UVIS)

- PSF RA – Right Ascension in degrees (WFC3/IR and WFPC2)

- PSF Dec – Declination in degrees (WFC3/IR and WFPC2)

- PSF Flux – Total flux in electrons (WFC3/IR is in electrons/s)

- Sky Level– Sky background counts per pixel around the PSF in electrons

- Qfit – Quality of the PSF fit in a unit-less scale from 0-1 (good-bad)

- Pixc – Central Pixel Flux in electrons (WFC3/IR is in electrons/s)

- MJD – Middle exposure time in MJD

- Date – MJD in date-time format (yyyy-mm-dd hh:mm:ss)

- Focus – HST Focus Model prediction at MJD in microns

The WFC3/UVIS, WFC3/IR, and WFPC2 databases contain around 24M, 5M, and 0.9M star images and measurements, respectively. The subsequent sections analyze the database and discuss statistical trends. Note that the analyses for flux, sky, Qfit, and pixc are performed in log space to better appreciate the distribution across the entire domain space. Table 3 summarizes the database's numerical data.

UVIS

	flux	sky	qfit	pixc	focus
count	2.383391e+07	2.383391e+07	2.383391e+07	2.383391e+07	2.383391e+07
mean	8.933740e+04	1.249731e+02	9.035508e-02	1.423917e+04	-9.949679e-01
std	7.016512e+04	1.070346e+03	7.644130e-02	1.091481e+04	2.919030e+00
min	1.000000e+00	-8.522410e+02	5.710000e-03	1.735000e+03	-1.304300e+01
25%	4.325500e+04	3.500500e+01	4.505000e-02	6.928800e+03	-2.929070e+00
50%	6.375300e+04	6.330700e+01	6.762000e-02	1.024650e+04	-9.560620e-01
75%	1.070760e+05	9.570300e+01	1.060600e-01	1.725890e+04	8.784450e-01
max	9.170890e+05	5.586710e+04	5.000000e-01	5.900050e+04	1.014970e+01

IR

	flux	sky	qfit	pixc	focus
count	4.911081e+06	4.911081e+06	4.911081e+06	4.911081e+06	4.911081e+06
mean	3.850032e+03	3.413101e+00	4.600763e-02	1.063615e+03	1.361794e-01
std	1.137372e+04	1.335702e+01	2.362242e-02	3.118907e+03	2.725873e+00
min	6.610000e+00	-3.000000e+00	-9.000000e-01	2.900000e+00	-1.331670e+01
25%	1.685900e+02	8.600000e-01	2.998000e-02	4.840000e+01	-1.714270e+00
50%	4.816300e+02	1.400000e+00	3.996000e-02	1.329000e+02	7.557950e-02
75%	1.706060e+03	2.700000e+00	5.476000e-02	4.746000e+02	1.971130e+00
max	1.735480e+05	1.870250e+03	1.500000e-01	3.000120e+04	9.510260e+00

WFPC2

	flux	sky	qfit	pixc	focus
count	891639.000000	891639.000000	891639.000000	891639.000000	242026.000000
mean	48039.351652	127.469942	0.103149	11278.683045	-3.234513
std	26051.942106	158.213579	0.030460	5730.890946	1.808467
min	13186.900000	-12.040000	0.013870	1886.300000	-14.704900
25%	27028.800000	43.630000	0.080300	6498.600000	-4.327240
50%	40629.800000	95.780000	0.106840	9779.300000	-2.975100
75%	63687.700000	162.380000	0.128880	15273.900000	-2.103720
max	223592.000000	5784.930000	0.150000	25001.500000	6.419940

Table 3: *Statistical summary of WFC3 and WFPC2 PSF database. Our numerical data included flux, sky, Qfit, pixc, and focus. The quantities and units were defined in a list at the beginning of Section 4. We display metrics of count (total number of samples in the database), mean, std (standard deviation), min, 25% (Q_1: lower quartile), 50% (median), 75% (Q_3: upper quartile), and max. WFC3's statistics were calculated on stars with focus measurements. WFPC2's statistics were calculated on all measurements except for focus since the Nulls were removed, hence why the counts are different. Since focus was not a direct measurement from PSF fitting and was uncorrelated with the other variables, removing Null samples gave us nearly identical statistics as keeping them.*
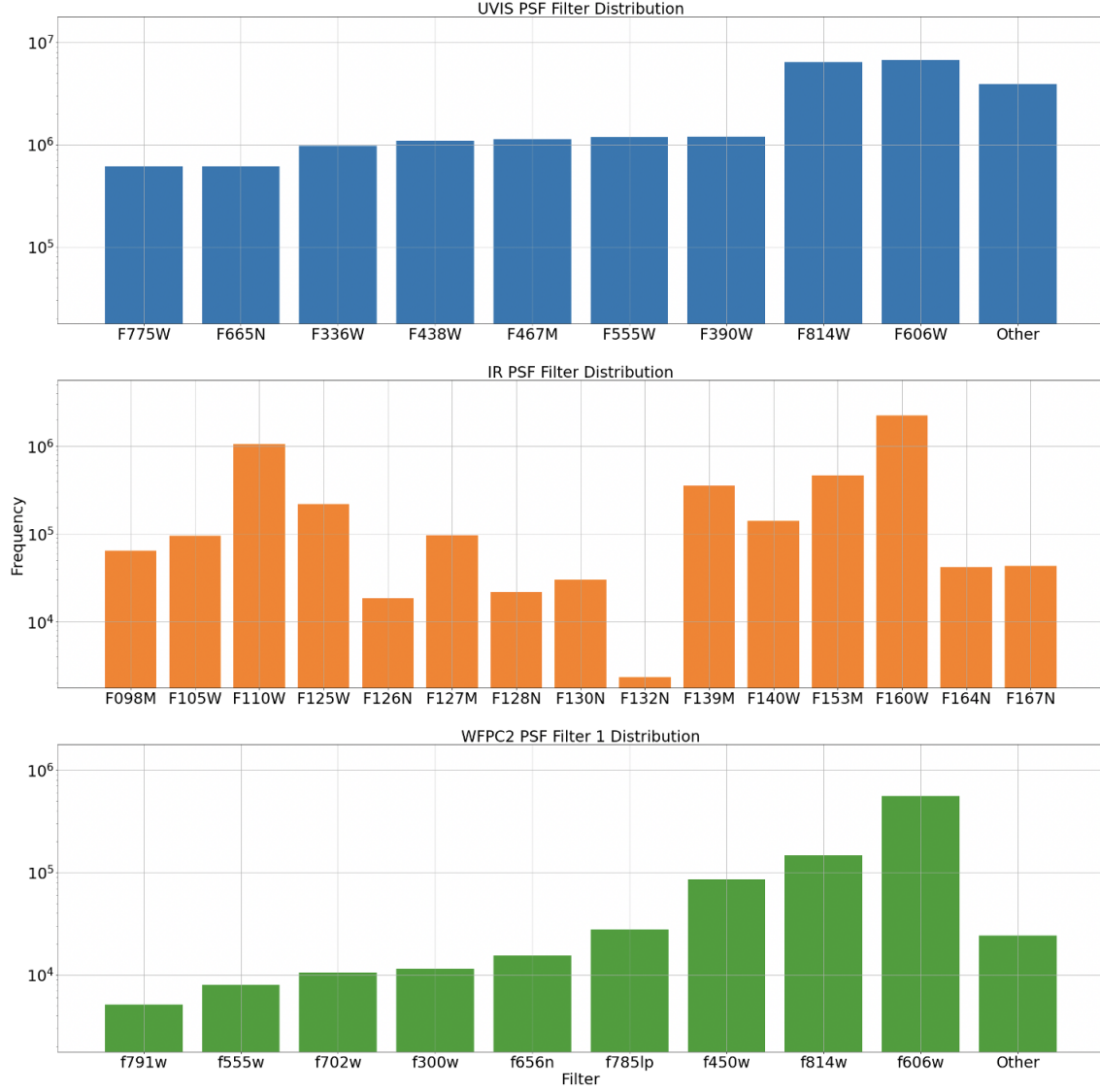
4.1. Filter and Aperture

Fig. 9.—*Frequency of filters used in the database. We determine frequency, or the number of stars found, by the routines across all observations in each filter. For UVIS, "Other" includes all the filters with $< 6 \times 10^5$ stars. For WFPC2, "Other" includes all the filters with $< 5 \times 10^3$ stars.*

4.1.1. Distribution of Stars by Filter

Out of the 62 WFC3/UVIS filters, the most stars were found in F606W, accounting for a little over a quarter (6.7M) of the database. The fewest number of stars found greater than zero (1142) was in F763M. Out of the 15 WFC3/IR filters, the most stars were found in F160W, accounting for around a little less than a half (2.3M) of the database. The fewest stars found (2340) was in F132N. Out of the 42 primary WFPC2 filters, the most stars were found in F606W, accounting for around three-fifths (0.6M) of the total number of stars identified in WFPC2 images. F343N had the fewest stars found (greater than zero) with just one measurement. WFPC2's secondary filter was rarely used. F791W, POLQ, and POLQN33 were used 5, 152, and 2 times, respectively. The rest of the observations used only one filter. We expected the wide-field filters to contain the most measurements because of their throughput and popularity among the astronomy community.

4.1.2. Distribution of Stars by Aperture

In WFC3/UVIS, the most stars were found in aperture UVIS-CENTER, accounting for a little over half (12.4M) of the database. This observation followed expectations because UVIS-CENTER uses the geometric center of the two CCD field of view as a reference point, which is optimal for most observations. The two WFC3/IR apertures, IR and IR-FIX, were used 49.3% and 50.7% of the time, illustrating no significant aperture preference. In WFPC2, WFALL had the most stars with around half a million measurements. This observation was expected because WFALL used all WFCs, which was optimal for most observations.
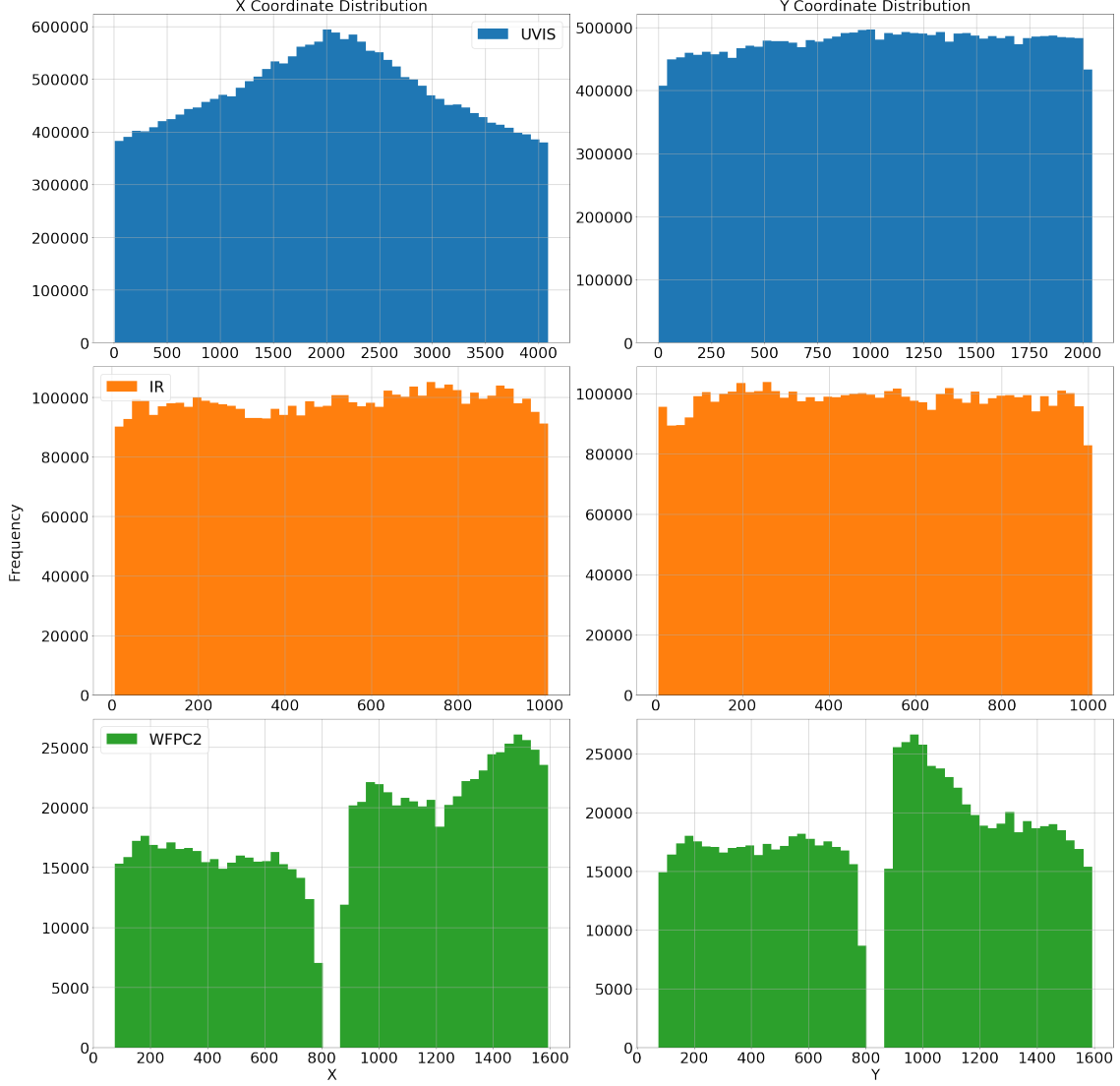
4.2. PSF Center and Celestial Coordinates

Fig. 10.—*WFC3/UVIS, WFC3/IR, and WFPC2 (top to bottom) PSF x-center (left) and y-center (right) coordinate distributions. The histograms illustrate global trends on the detectors. The x-axis is the center x/y pixel location of the stars on the detector, and the y-axis is the frequency, or number of stars observed. Stars identified in WFC3/UVIS images were centered along the x-axis and uniform across the y-axis. Stars identified in WFC3/IR images were identified relatively evenly by x-coordinate, with the minor dips caused by the detector defects. WFPC2's split in both axes illustrates the distinguished four chips. The smaller distributions were caused by PC, which was expected due to its physically smaller size.*

The x-center coordinate distribution of stars identified in WFC3/UVIS images was unimodal around the middle of both chips with a linear decrease toward both ends of the chips. This feature was expected due to the abundance of UVIS-CENTER observations, where sources are more likely to be centered. The y-center coordinate distribution was relatively uniform with no preference in location along the y-axis. The WFC3/IR x-center coordinate and y-center coordinate distributions were relatively uniform. The WFPC2 x-center coordinate and y-center coordinate distributions followed two distributions before and after the middle of the detector (pixel 800). Since the camera had four separate chips, there were gaps in the center of both axes of WFPC2. The Wide Field Cameras (WFCs) contained more observations than the Planetary Camera (PC) due to the platescale differences and WFCs' field-of-views being four times larger than PC. The x-center coordinate and y-center coordinate distributions on all four chips were relatively uniform. The x-center coordinate distributions of WF2 and WF3 were bimodal centered around 1000 and 1500 and the y-center coordinate distributions of WF3 and WF4 were unimodal centered around 900.
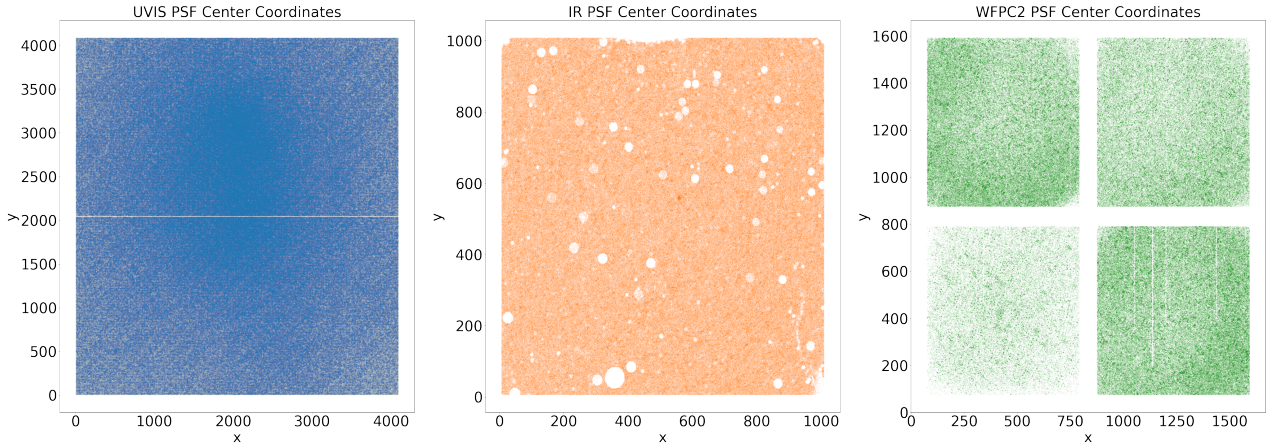

Fig. 11.—*WFC3/UVIS, WFC3/IR, and WFPC2 detector maps (left to right). The figure shows each star's location on the detectors. WFC3/UVIS was relatively even with a slight skew towards the top CCD chip UVIS1. The holes in WFC3/IR were caused by blobs and other image defects. The WFCs had higher star counts than PC in WFPC2. This is expected since the PC has a smaller pixel scale such that its field-of-view (35") is one fourth that of the WFCs (150").*

By plotting the coordinates of each measurement, we visualize the database distribution on the detectors (see Figure 11). In WFC3/UVIS, the density was slightly skewed towards top CCD chip UVIS1, which contains 53% of the sources. The other 47% of the sources were on the bottom CCD chip UVIS2, indicating that the two chips observed similar number

of stars. The WFC3/IR has multiple defects that are visible in the detector plots. The largest hole on the bottom left is the death star, which is a region of dead and unstable pixels (Sunnquist 2019). The feature on the lower right is the wagon wheel, which is a region of pixels with lower than normal quantum efficiency (Sunnquist 2019). At the top middle are unbonded pixels and the rest of the holes are prominent blobs (Pirzkal 2010). Since these chip defects block flux, it was expected that there wouldn't be any sources in those locations. The bottom left of the WFPC2 CCD chips is PC, which has a lower source count than the WFC chips. Just as in the histograms, this effect was expected due to the different platescales of the cameras and the effect of the severe-undersampled PSF.

Since the WFC3/IR and WFPC2 pipelines recorded RA and Dec, we illustrate the positions on the sky of our database and the relative star densities (see Figure 12 and 13). These figures display our database's most popular and star abundant objects. Unfortunately, we were not able to produce a similar plot for UVIS because the RA and Dec were not recorded for the database. The density map is binned by integer degrees and the color map is log scaled. Circled are the locations with the highest star densities. For WFC3/IR, the densest objects included Andromeda Galaxy, 47 Tucanae (47TUC), omega Cen, Westerlund 1, Sagittarius A* (Sgr A*), and Caldwell 93 (NGC 6397). For WFPC2, the densest objects included Messier 22 (M22), 47TUC, omega Cen, Sgr A*, the Large Magellanic Cloud (LMC) and the Small Magellanic Cloud (SMC). These results were expected because all of these objects are either globular clusters or galactic nuclei, which have high star densities and are frequently observed by the astronomical community.
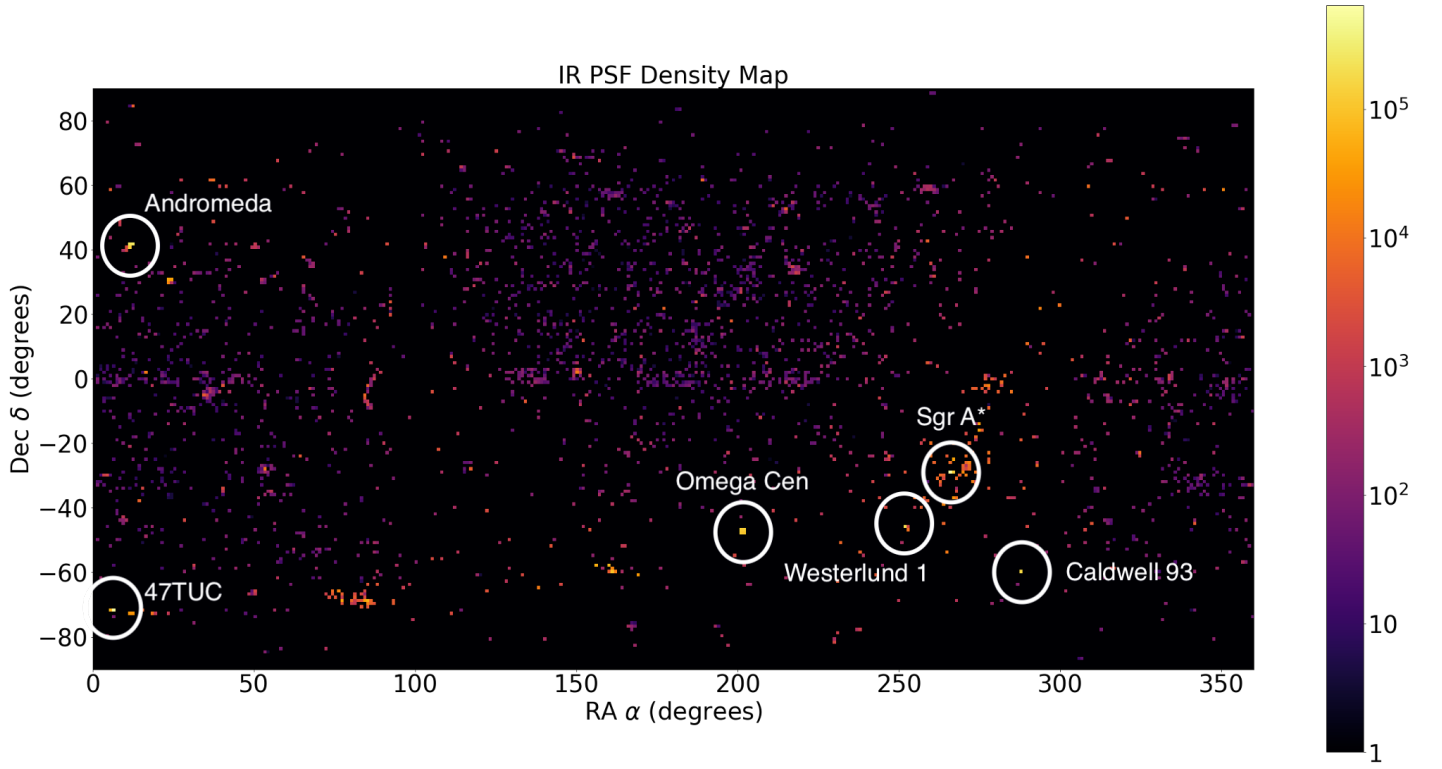
Fig. 12.—*WFC3/IR PSF celestial coordinates map. Each pixel is one square degree, integer spaced. The x-axis and y-axis are angles of right ascension and declination, respectively. The color map is log scaled so less dense regions appear. Regions with greater than 10^5 sources are circled, which are popular, star-abundant objects.*
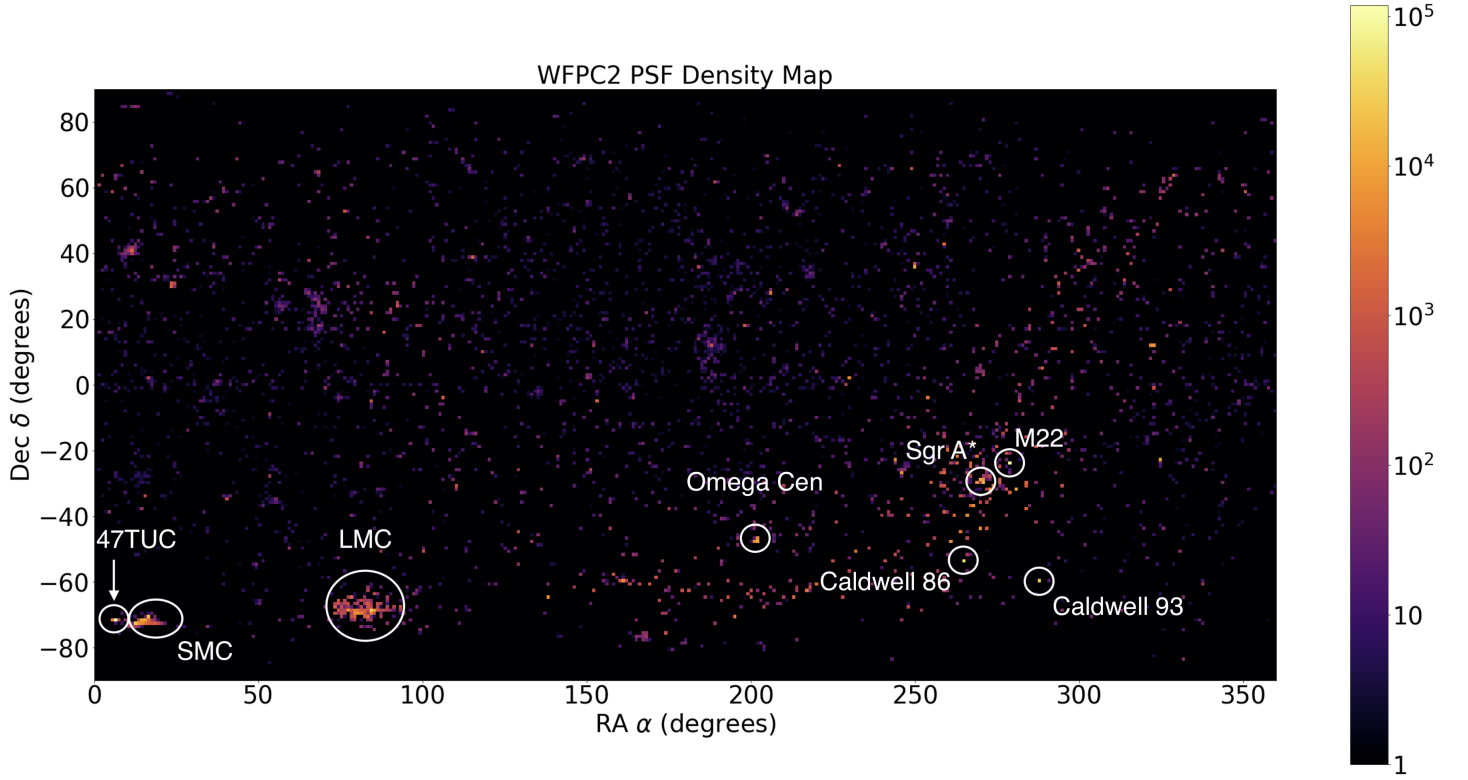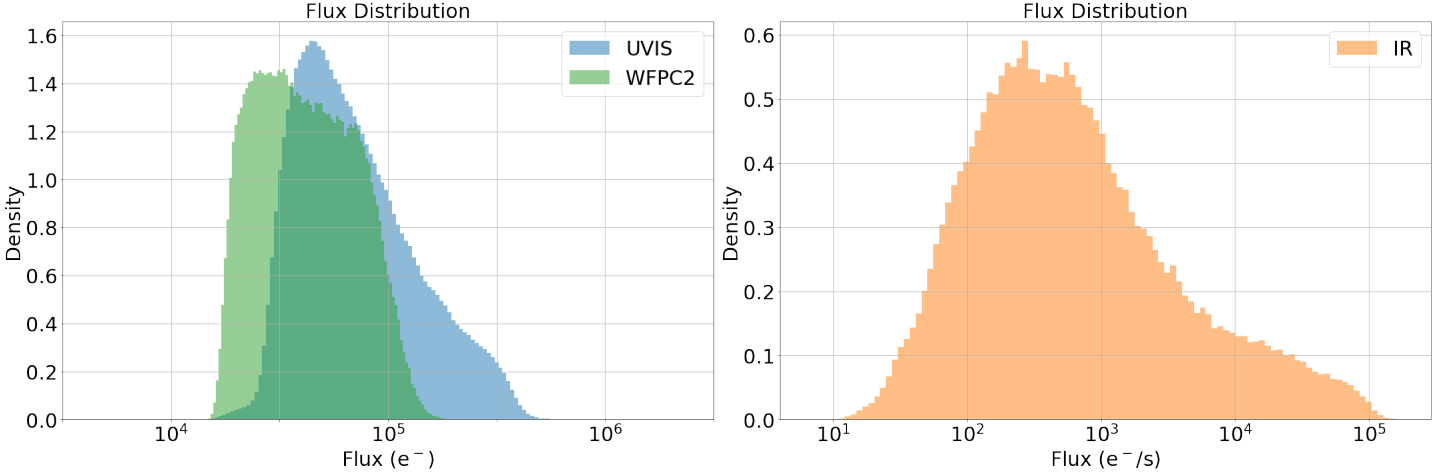
Fig. 13.—*WFPC2 PSF celestial coordinates map. Each pixel is one square degree, integer spaced. The x-axis and y-axis are angles of right ascension and declination, respectively. The color map is log scaled so less dense regions appear. Regions with greater than 10^4 sources are circled, which are popular, star-abundant objects.*

4.3. Total Flux

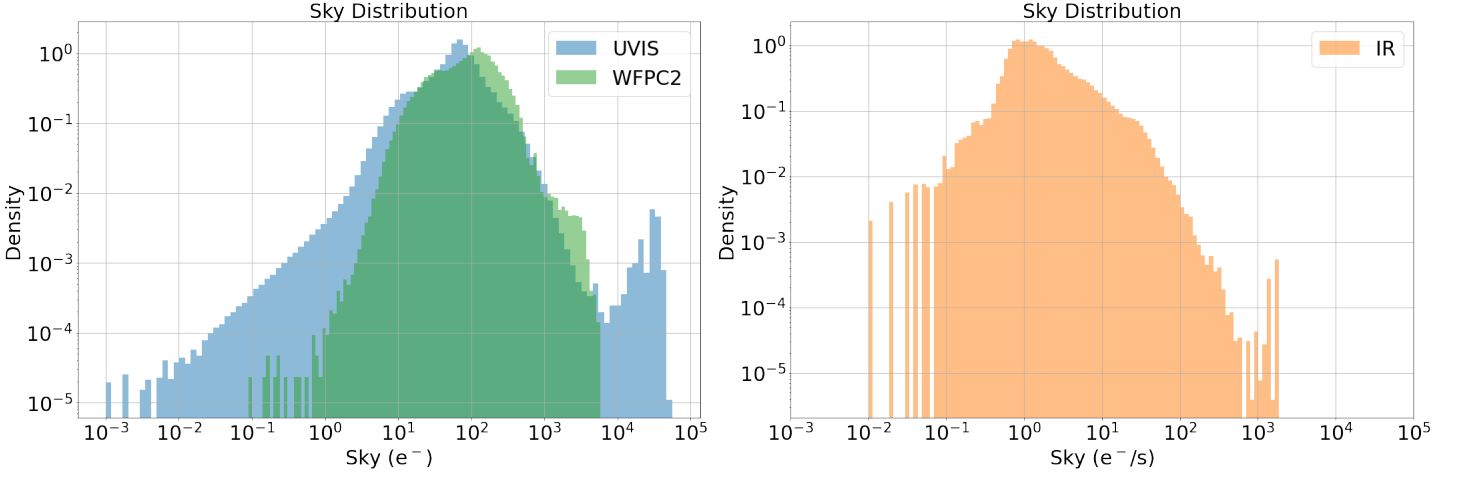
Fig. 14.—*WFC3 and WFPC2 flux distributions. The y-axis is density, which is normalized frequency and makes the integral of each curve equal to one. WFC3/IR was measured in e^-/s while the other two detectors were measured in e^-. The 314 WFC3/UVIS observations that were less than 10^4 e^- are not shown.*

The distributions of total flux per star were normal with a right skew. [1] As a rough approximation, we expected the flux distributions to follow a power law in linear space. If we assumed all stars had roughly the same luminosity and were uniformly distanced, then flux would follow a power law. WFC3/UVIS and WFPC2 were centered around 6×10^4 and 2.5×10^4 e^-, respectively, while WFC3/IR was centered around 6×10^2 e^-/s. There were 307 objects in UVIS with flux $= 1$ e^-. An investigation of these objects presented no patterns, indicating a possible software error in flux calculations.

---

[1]Note a normal distribution in log space approximates to a power law in linear space.

4.4.   Sky Level

Fig. 15.—*WFC3 and WFPC2 sky distributions. The y-axis is density, which is normalized frequency and makes the integral of each curve equal to one. WFC3/IR was measured in e^-/s while the other two detectors were measured in e^-. The increase in density at the extreme ends of the distributions are skewed by dozens of outlier images.*

Sky-level is the sky background counts per pixel around the PSF. The sky-level distributions roughly followed irregular normal distributions. WFC3/UVIS and WFPC2 were both centered around 100 e^-, and WFPC2 was centered around 40 e^-/s. WFC3/UVIS had the widest spread in sky levels. There were approximately 61K objects with negative sky levels in WFC3/UVIS. These measurements were caused by excessively saturated stars. In addition, the WFC3/UVIS observations with sky levels greater than 10^4 e^- were calibration images and planetary images. There were 334 observations with negative sky levels in WFC3/IR with no simple pattern explaining why. The WFC3/IR observations with sky levels greater than 10^3 e^-/s were images of clusters NGC 3603 and Terzan 5. There were 20 objects with negative sky levels in WFPC2. Determining any global patterns for negative sky levels will be left as future work.

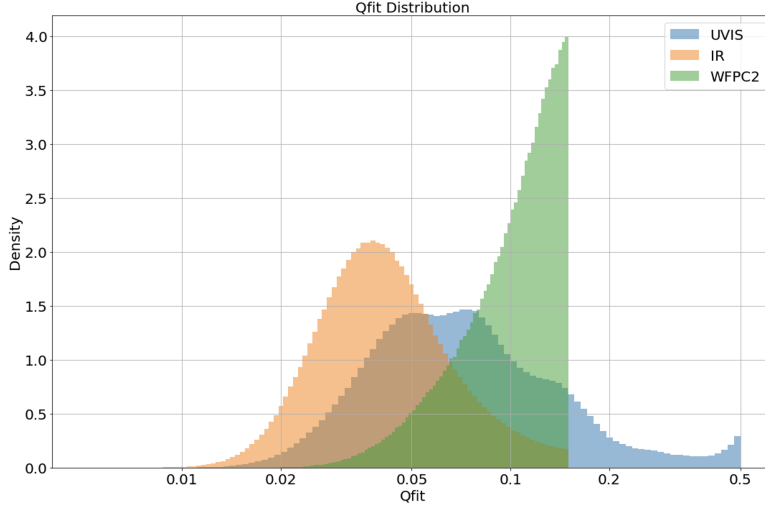## 4.5. Quality of Fit (Qfit)

Fig. 16.—*WFC3 and WFPC2 Qfit distributions (binned in log-space). The y-axis is density, which is normalized frequency and makes the integral of each curve equal to one. Smaller Qfit values indicate better fits. WFC3/UVIS has the widest distribution, WFC3/IR has the most "normal" distribution, and WFPC2 continuously increases to the cutoff. WFC3/UVIS's upper limit of 0.5, and WFC3/IR's and WFPC2's upper limit of 0.15 are illustrated at the right tail of each distribution.*

WFC3/UVIS Qfit was approximately a right skewed normal distribution with a mean of 0.090±0.076. There was also a local maximum at 0.5, which was a clipping value. The right skew validates the trust in our PSF models because a majority of the measurements were less than 0.1, indicating good fits. 47 objects, most of which were saturated stars, had a Qfit of 0.5. There were no immediate patterns as to why there was a local minimum at 0.4, but the minimum could serve as an empirical clipping value for future fits.

The WFC3/IR Qfit distribution was normal, unimodal, centered about 0.046±0.024, and slightly skewed to the right. The cutoff at 0.15 illustrates the restrictions on star candidates determined by the pipeline. Overall, the WFC3/IR models fit better than the WFC3/UVIS models since the WFC3/IR peak is closer to 0. There were 31 stars at the cutoff value, but appeared to be in good images. There was one negative Qfit of -0.9 in LMC image, but was likely caused by bad pixels.

WFPC2 Qfit did not follow any distribution and continuously increased to the cutoff value of 0.15. This distribution's mean was 0.103±0.030. Since the distribution mono-tonically increases, this may indicate the WFPC2 fits were generally weaker than WFC3.

Adopting a more generous max clipping Qfit will provide more insight on the distribution as a whole and if the fits were actually weaker.
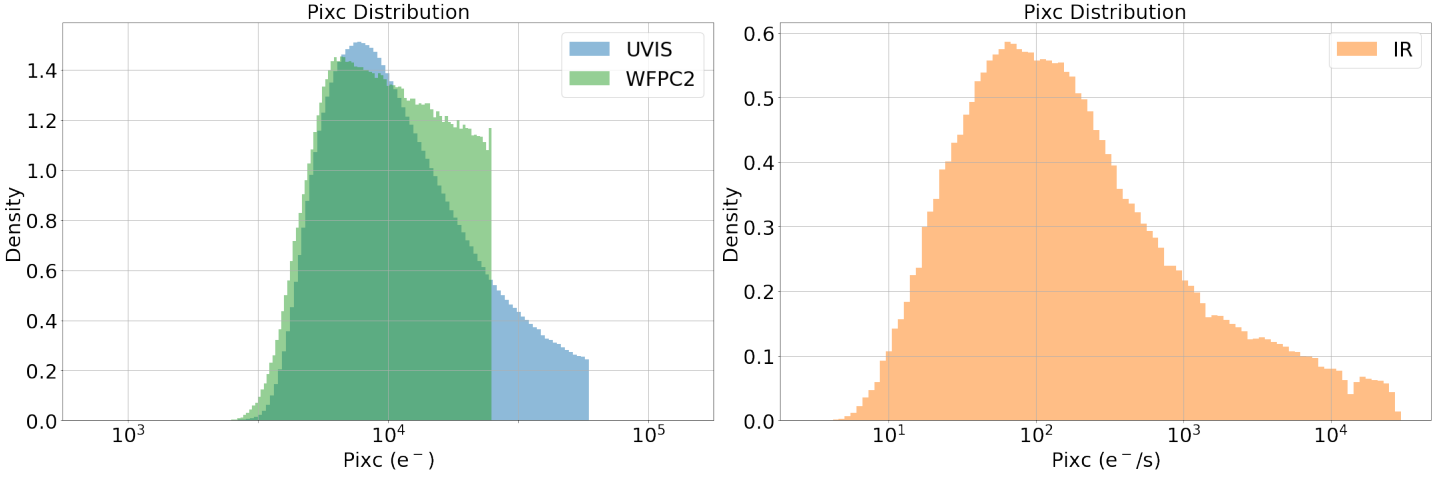
4.6. Center Pixel Flux (Pixc)

Fig. 17.—*WFC3 and WFPC2 pixc distributions. The y-axis is density, which is normalized frequency and makes the integral of each curve equal to one. The distributions were similar to flux except for hard cutoffs of 5.9×10^4 e^- for UVIS and of 2.5×10^4 e^- for WFPC2.*

Pixc followed a similar distribution to that of the flux. This relationship was expected because of the positive correlation between the center pixel flux and total flux; flux should increase as pixc increases. WFC3/UVIS and WFPC2 were both centered around 6×10^3 e^-, and WFC3/IR was centered around 1×10^2 e^-/s. WFC3/UVIS's hard cutoff at 5.9×10^4 e^- corresponds to the saturation level, which varies slightly across the detector. Unlike the WFC3/UVIS, the observational strategy in the WFC3/IR allows for resetting of the detector during an exposure, which explains the continuous decrease in pixc instead of the hard drop off.
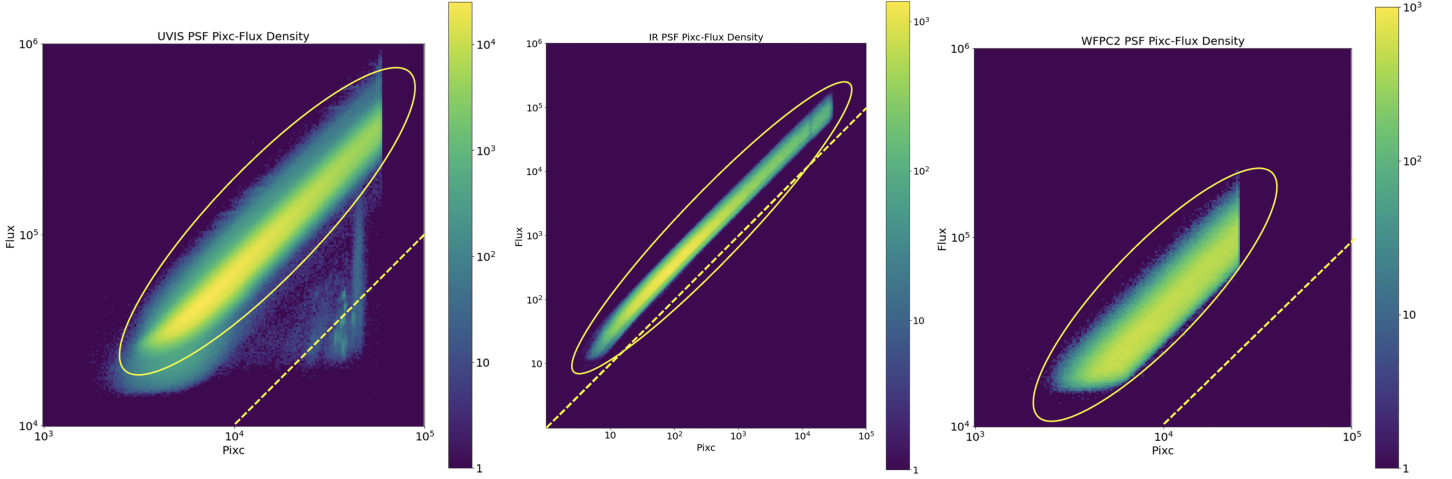
Fig. 18.—*WFC3/UVIS, WFC3/IR, and WFPC2 (left to right) pixc-flux correlations. The color map is log scaled, representing the density of PSFs fitted with those measurements. The dashed yellow line is where pixc = flux. WFC3/IR and WFPC2 were well above that threshold, but approximately 14K observations in WFC3/UVIS were not. Circled is the main linear trend. WFC3/IR and WFPC2 did not have deviations outside their respective regions, but WFC3/UVIS did.*

We compare the central pixel and total flux values to determine the tightness of the correlation for each detector (see Figure 18). WFC3/IR and WFPC2 had Pearson Correlation Coefficients (PCC) of 0.977 and 0.908, respectively, and total flux was always greater than pixc when fitting PSFs. WFC3/UVIS's PCC (0.966) was greater than WFPC2 due to the database size being 20 times larger, allowing overall statistics to become overwhelmingly dominant. In addition, WFC3/UVIS was a wider spread and thousands of fits had the central pixc greater than total flux in WFC3/UVIS. This error may be caused by cosmic rays and/or warm/hot pixels. Parts around those pixels were most likely oversubtracted in `img2xym_wfc3uv`, making the stars' total fluxes less than the central pixel fluxes. Calibration images containing no objects seemed to cause these anomalous "stars". We plan to continue investigating this feature in the database as future work.
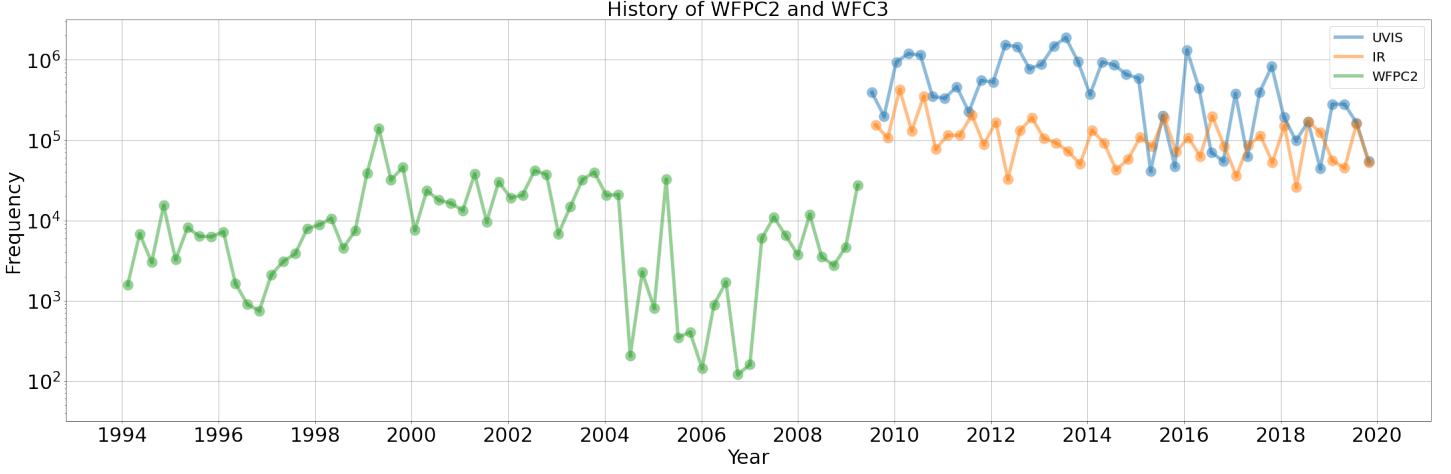
4.7. Observation Time

Fig. 19.—*Usage of WFC3 and WFPC2 over time. Each data point represents the number of stars observed during a season (winter, spring, fall, or summer) in a specified detector. By seeing the various increases and decreases in stars observed, we gained insight on each instrument's history in the scientific community.*

The usage of each detector is shown in Figure 19. WFC3/UVIS's most and least popular seasons occurred in Summer 2013 and Spring 2015, respectively. WFC3/IR's most and least popular seasons were Winter 2010 and Spring 2018, respectively. HST was in safe mode during Fall 2018, which explains the substantial decrease in number of stars observed in WFC3/UVIS during that time period. WFPC2's most and least popular periods were Spring 1999 and Fall 2006, respectively, with a spike at the end of its mission in Spring 2009.
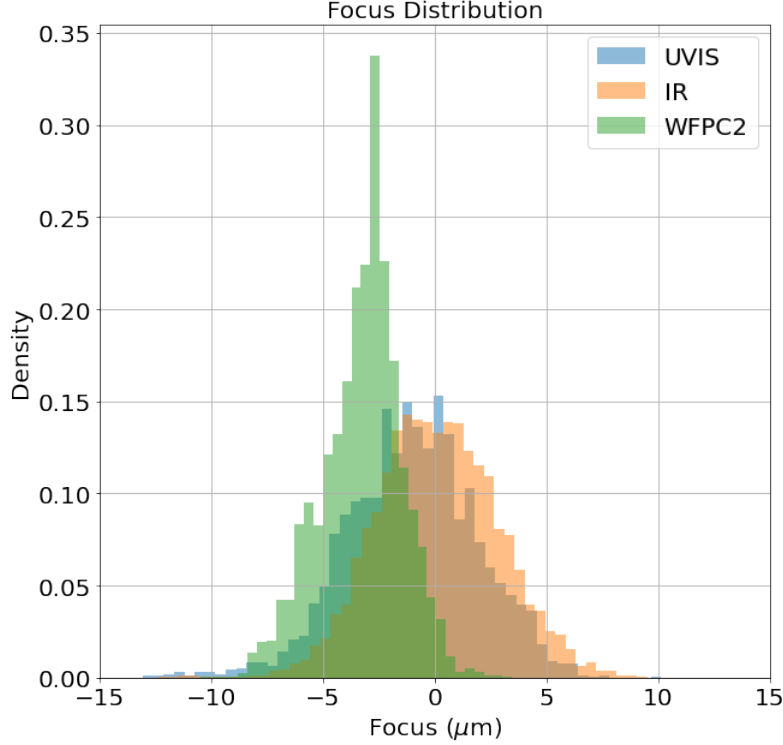
4.8. Focus

Fig. 20.—*WFC3 and WFPC2 focus distributions. All distributions were normal with WFPC2 having a smaller standard deviation of 1.81 versus WFC3/UVIS and WFC3/IR's standard deviations of 2.91 and 2.73, respectively. WFPC2 also had a slight shift towards negative focus values, which was consistent with the parent distribution.*

The focus distributions were normal, which was expected since focus was pulling from a parent normal distribution. WFC3/UVIS, WFC3/IR, and WFPC2 were centered around -0.99, 0.14, and -3.23 microns respectively. We expected WFPC2 to be centered around a negative focus instead of zero because the parent distribution from 2003-2009 was centered around a negative focus (see Figure 7). There were approximately 4×10^4 and 2.1×10^4 Null observations in WFC3/UVIS and WFC3/IR respectively. Again, the Null focus values were due to images being observed in one of the focus model's gaps (see Figure 8). These stars were removed from the database. In WFPC2, only a little over a quarter (0.24M) had estimated focus values with the rest being Null. This feature was expected because that quarter was observed in 2003 onward, which contained available focus model data. Since the majority of samples had Null focus values, we kept them in the database. The Null values also did not affect the overall statistics of the WFPC2 database.

5. Retrieving PSFs through MAST Archive

The observed WFPC2/WFC3 PSFs are searchable through STScI MAST archive website (https://mast.stsci.edu/portal/Mashup/Clients/Mast/Portal.html). The procedure is as follows:

- To access the WFC3 PSF databse, select "WFC3 PSF" under "Select a collection" (A similar option will be available soon for the WFPC2 database, which is under construction as of this writing in May 2021).

- Choose either UVIS or IR (for WFC3) to access the appropriate database (as shown in the top panel of Fig 20).

- Choose "Advanced Search" option to select specific PSF parameters to search the database (as shown in the bottom panel of Fig. 20). Note that there is a pre-selected "Good Quality PSF Subset" consisting of less than 100 PSFs, which may serve as a guide to select the various parameters.

The results can then be exported as a table, or displayed as a "grid," with the option to view as a list or as an album. The users can then download the actual a 21x21 pixel cutout of the PSFs, or they can download the entire images. There are several options to facilitate quick inspection of the data, which include downloading the list as table to a local file, or viewing the charts for the selected data. The PSF tables can also be cross-matched with other catalogs, which may be very useful for other astronomical applications.

A unique feature of the PSF database is that the images and cutouts are generated on-the-fly, taking only the PSF parameters described above. This ensures that (i) the input searchable database remains small, consisting of a single file where the parameters of each PSF occupy a single line, and (ii) the actual images and PSFs take the most up-to-date pipeline calibrations into account since the PSF cutouts and images are generated on-the-fly through MAST archive.

6. Discussions and Future Work

Many astronomical projects benefit from better characterized PSFs. We list below a few such projects (by no means exhaustive) where a well-characterized PSF plays a critical role in producing outstanding results:

- **Morphology of High Redshift Galaxies** There is considerable interest in morphological study of galaxies at high redshift, particularly of star-forming galaxies (e.g.
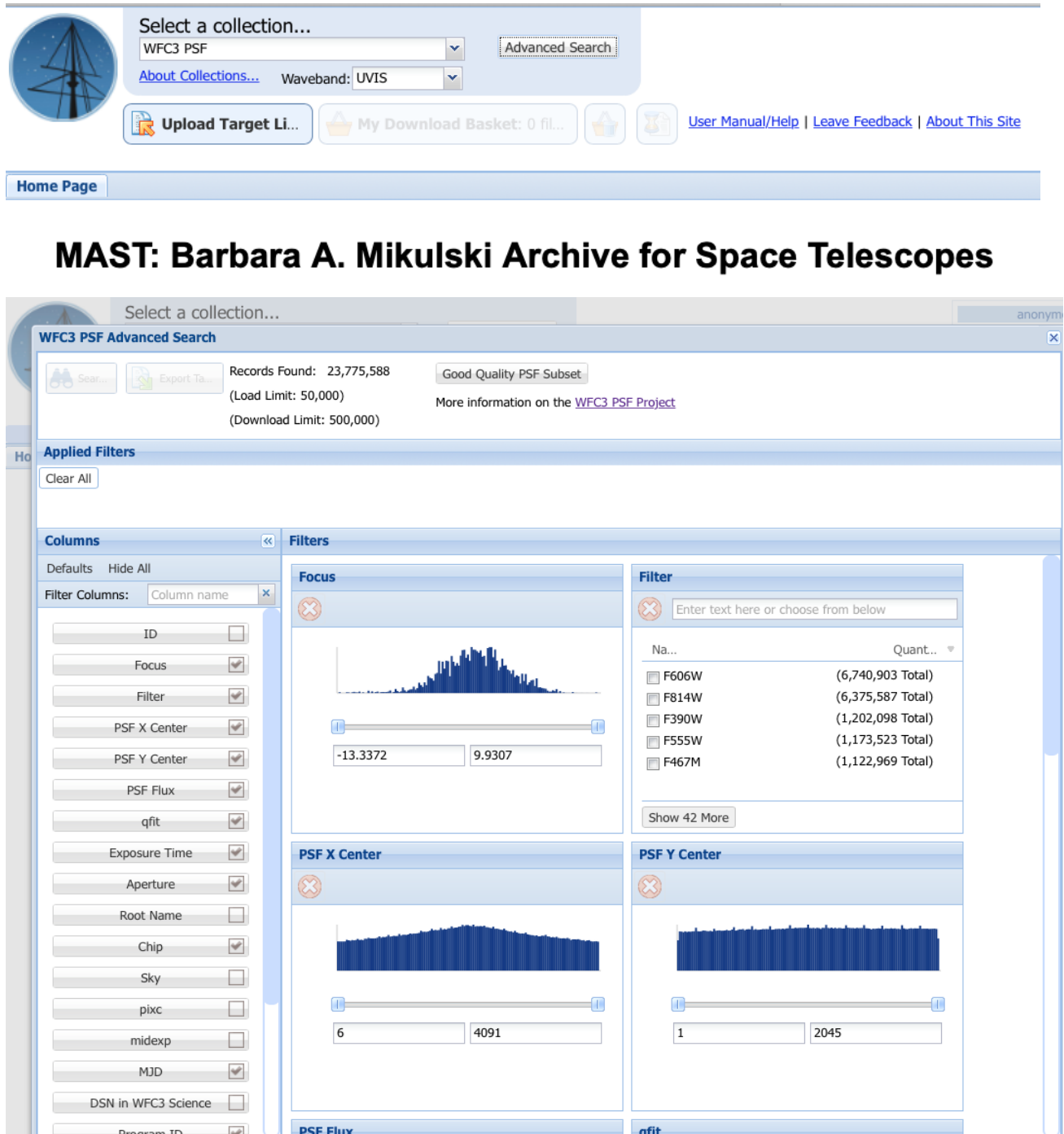
Fig. 21.—*A view of the MAST PSF search tool, showing the search page (top), and the details of a selected sample of PSFs*

Law et al 2012). These studies require convolving the galaxy models (such as Sersic models) with the observational PSFs to derive the light profile and other statistics, and to determine if the star formation is caused by galaxy merging or if it is intrinsic.

- **Mass Distributions of Lensing Clusters of Galaxies**: There are several high-profile HST projects, such as the Cluster Lensing And Supernova survey with Hubble (CLASH), which is a 524-orbit Multi-Cycle Treasury Program. This program uses the gravitational lensing properties of 25 galaxy clusters to accurately constrain their mass distributions (Postman et al. 2012) through detailed modeling of the observed shapes of the lensed galaxies. In order to determine the mass distributions of the galaxies, the observed PSFs (similar to the ones presented here) need to be convolved with empirical shapes to reproduce the observed shapes.

- **Detection and Characterization of Exoplanets and Disks**: Soummer et al. (2012) devised a new method to achieve PSF subtractions for high-contrast imaging using principal component analysis that is applicable to both point sources or extended objects (disks). They use a libray PSF, similar to the one presented here, to create an orthogonal basis of eigenimages on which the science target is projected. Using this method, they discovered several new debris-disks around main-sequence stars (Soummer et al. 2014).

- **Crowded-Field Photometry of faint stars**: The accurate photometry of the stars in the SWEEPS field imaged with WFC3 was used to detect the white dwarf cooling sequence in the galactic bulge (Calamida et al. 2014). This project needed both accurate photometry and proper motions of the faint white dwarfs in this crowded field. Since the white dwarfs are faint and the field is crowded, a good knowledge of the PSFs was crucial for this project. This new and interesting study generated a strong interest in the astronomical circles and the popular media.

- **Multiple Sequences in Globular clusters through Crowded Field Photometry and Astrometry:** A good knowledge of the PSF is crucial for accurate photometry in crowded fields. In globular cluster studies, the PSF helps in determining accurate positions of the stars, which can then be used to determine their proper motions using images taken at multiple epochs. The combination of these two have proven very powerful in discovering mulitple sequences in globular clusters, which has revolutionized this field (e.g. Piotto et al. 2012, Bellini et al. 2017).

- **Measurement of Relativistic Deflection:** Recently, the nearby white dwarf (WD) Stein 2051B passed in front of a faint background star, causing a relativistic deflection of the background star. Sahu et al. (2017) measured the relativistic deflection caused

by the white dwarf—the first such measurement of deflection caused by a star outside the solar system—and thereby determined the mass of the WD. This work was listed by Discover magazine as one of the Top 100 Science Stories of 2017. Measuring the tiny deflection of the faint background star was challenging since the background star is about 400 times fainter than the nearby white dwarf. It was important to subtract the PSF of the white dwarf correctly, for which a good knowledge of the PSF was crucial.

The first three projects from the above list need simple observational PSFs for the particular observational scene. This database serves as an excellent resource in such cases. The last three projects from the above list need "super samples PSFs" constructed from a set of dithered images, a set of which are currently available in the WFC3 PSF website. However, the PSFs available so far cover a subset of most used filters. In absence of good empirical PSFs, users have often used TinyTim. However, since TinyTim is purely model based, it often does not fully represent the observational scene. Users can use the PSF database described here to create their own supersampled PSFs, as appropriate for their particular filter, focus level, etc. In future, we plan to provide tools to use these PSFs for specific cases.

7. Conclusions

A considerable amount of HST science involves analyzing images of stars. We present a database of all the available observed WFPC2 and WFC3 UVIS/IR stellar PSFs. The database contains 30M well-measured stellar objects and is now publicly available on MAST. We describe the statistical properties of this dataset (position, quality of fit, flux distribution, etc.). The mean quality of fits, or fractional disagreement between the model and image pixels, were 0.103±0.030 (WFPC2), 0.090±0.076 (WFC3/UVIS), and 0.046±0.024 (WFC3/IR). Accurate PSFs have been used in many astronomical projects leading to very interesting results, such as crowded-field photometry and precise astrometry. This database will be very useful for all such projects. In future, we plan to provide some additional tools to use the PSF database for astronomical applications.

References

Anderson J., King I., 2000, "Toward High-Precision Astrometry with WFPC2. I. Deriving an Accurate PSF", PASP, 112, 1360.

Anderson J., King I., 2006, "PSFs, Photometry, and Astrometry for the ACS/WFC", ACS-ISR 2006-01.

Anderson J., 2016. "Empirical Models for the WFC3/IR PSF", WFC3-ISR 2016-12.

Anderson J., 2018, "Focus-Diverse PSFs for Five Commonly Used WFC3/UVIS Filters", WFC3-ISR 2018-14.

Bellini A., Milone A. P., Anderson J., et al., 2017, "The State-of-the-art HST Astro-photometric Analysis of the Core of Omega Centauri. III. The Main Sequence's Multiple Populations Galore", ApJ, 844, 164.

Calamida A., Sahu K. C., Anderson J., et al., 2014, "First Detection of the White Dwarf Cooling Sequence of the Galactic Bulge", ApJ, 790, 164.

Dalcanton J. J., Williams B. F., Lang D., et al., 2012, "The Panchromatic Hubble Andromeda Treasury", ApJS, 200, 18.

Dressel L., 2012, "Breathing, Position Drift, and PSF Variations on the UVIS Detector", WFC3-ISR 2012-14.

Dressel L., 2021, "Wide Field Camera 3 Instrument Handbook for Cycle 29, Version 13.0", WFC3-IHB.

Krist J., 2003, "ACS WFC & HRC field independent PSF variations due to optical and charge diffusion effects", ACS-ISR 2003-06.

Law D. R., Steidel C. C., Shapley A. E., et al., 2012, "An HST/WFC3-IR Morphological Survey of Galaxies at z = 1.5-3.6. I. Survey Description and Morphological Properties of Star-forming Galaxies" ApJ, 745, 85.

McMaster M., Biretta J., 2010, "Wide Field and Planetary Camera 2 Instrument Handbook, Version 10.0", WFPC2-IHB.

Nino D. D., Makidon R. B., Lallo M., et al., 2008, "HST Focus Variations with Temperature", ACS-ISR 2008-03.

Piotto G., Milone A. P., Anderson J., et al., 2012, "Hubble Space Telescope reveals multiple Sub-Giant Branch in eight Globular Clusters", ApJ, 760, 39.

Pirzkal N., Viana A., Rajan A., 2010, "The WFC3 IR "Blobs",
    WFC3-ISR 2010-06.

Postman M., Coe D., Benítez N., et al., 2012, "The Cluster Lensing and Supernova Survey
    with Hubble: An Overview", ApJS, 199, 25.

Sabbi E., Bellini A., 2013, "UVIS PSF Spatial and Temporal Variations",
    WFC3-ISR 2013-11.

Sahu K. C., Anderson J., Casertano S., et al., 2017, "Relativistic deflection of background
    starlight measures the mass of a nearby white dwarf star", Sci, 356, 1046.

Soummer R., Pueyo L., Larkin J., 2012, "Detection and Characterization of Exoplanets and
    Disks Using Projections on Karhunen-Loéve Eigenimages", ApJL, 755, L28.

Soummer R., Perrin M. D., Pueyo L., et al., 2014, "Five Debris Disks Newly Revealed in
    Scattered Light from the Hubble Space Telescope NICMOS Archive", ApJL, 786, L23.

Sunnquist B., Brammer G., Baggett S., 2019, "Time-dependent WFC3/IR Bad Pixel Ta-
    bles", WFC3-ISR 2019-03.